with a technique requiring only fractions of a milliliter. The rest of the samples are divided into two parts and are handled the same way as the larger samples described previously. This makes this method very practical for quantitative FDG studies on children, especially small children and newborns.

A semidynamic study based on two scan points, the first at 10–20 min and the second at 45–60 min postinjection, could be analyzed with the graphic method described by Patlak et al. (*12*), requiring only two blood samples that are treated as described previously. This simplified Patlak analysis will be validated in another study.

CONCLUSION

A new method to normalize clinical routine FDG studies based on only one venous blood sample is presented. The method has been validated against a standard method with multiple blood samples showing an accuracy of better then ± 8%.

ACKNOWLEDGMENTS

The authors thank Hans Lundqvist, PhD, Uppsala University and Mario Monti, Professor, University Hospital Lund, for helpful discussions. This work has been supported by grants from the Swedish Cancer Foundation grant 3320-B95-04XAB; the Gunnar, Arvid and Elisabeth Nilsson Foundation; the Mrs. Berta Kamprad Foundation; the John and Augusta Persson Foundation; the Royal Physiographic Society; the Lund University Medical Faculty; and the Lund University Hospital Fund.

REFERENCES

1. Phelps ME, Huang SC, Hoffman EJ, et al. Tomographic measurement of local cerebral glucose metabolic rate in humans with (F-18)2-fluoro-2-deoxy-D-glucose: validation of method. *Ann Neurol* 1979;6:371–388.
2. Germano G, Chen BC, Huang S-C, Gambhir SS, Hoffman EJ, Phelps ME. Use of the abdominal aorta for arterial input function determination in hepatic and renal PET studies. *J Nucl Med* 1992;33:613–620.
3. Takikawa S, Dhawan V, Spetsieris P, et al. Noninvasive quantitative fluorodeoxyglucose PET studies with an estimated input function derived from a population-based arterial blood curve. *Radiology* 1993;188:131–136.
4. Lindholm P, Minn H, Leskinen-Kallio S, et al. Influence of the blood glucose concentration on FDG uptake in cancer—a PET study. *J Nucl Med* 1993;34:1–6.
5. Langen K-J, Braun U, Rota Kops E, et al. The influence of plasma glucose levels on fluorine-18-fluorodeoxyglucose uptake in bronchial carcinomas. *J Nucl Med* 1993;34: 355–359.
6. Fischman AJ, Alpert NM. FDG-PET in oncology: there's more to it than looking at pictures. *J Nucl Med* 1993;34:6–11.
7. Chaiken L, Rege S, Hoh C, et al. Positron emission tomography with fluorodeoxyglucose to evaluate tumor response and control after radiation therapy. *Int J Radiat Oncol Biol Phys* 1993;27:455–464.
8. Brooks RA. Alternative formula for glucose utilization using labeled deoxyglucose. *J Nucl Med* 1982;23:538–539.
9. Rhodes CG, Wise RJS, Gibbs JM, et al. In vivo disturbance of the oxidative metabolism of glucose in human cerebral gliomas. *Ann Neurol* 1983;14:614–626.
10. Monti M, Wadsö I. Microcalorimetric measurements of heat production in human erythrocytes. IV. Comparison between different calorimetric techniques, suspension media, and preparation methods. *Scand J Clin Lab Invest* 1976;36:573–580.
11. Monti M, Wadsö I. Microcalorimetric measurements of heat production in human erythrocytes. III. Influence of pH, temperature, glucose concentration, and storage conditions. *Scand J Clin Lab Invest* 1976;36:565–572.
12. Patlak CS, Blasberg RG, Fenstermacher JD. Graphical evaluation of blood-to-brain transfer constants from multiple-time uptake data. *J Cereb Blood Flow Metab* 1983;3:1–7.

Photon Energy Recovery: A Method to Improve the Effective Energy Resolution of Gamma Cameras

Pascal P. Hannequin and Jacky F. Mas

Centre d'Imagerie Nucléaire, Annecy; and Service de Médecine Nucléaire, Epinal, France

One of the major limitations of gamma cameras is their relatively poor energy resolution. The main practical consequence of this is that the detection of both scattered and unscattered photons in the photopeak energy window, affecting image contrast and resolution, makes the data inconsistent with the assumption of scatter-free projection data in reconstruction and attenuation correction algorithms. Here, we proposed a method to improve the effective energy resolution of scintigraphic acquisitions. This method is called photon energy recovery (PER). **Methods:** Photon energy recovery is based on a spectral deconvolution analysis and uses iterative recurrent linear regressions. In practice, PER only required splitting the photopeak energy window into several subwindows and did not need list mode acquisitions. The method was fully automated. Photon energy recovery was quantitatively validated on ^{99m}Tc planar images using a Monte Carlo simulation and a real phantom and was illustrated by a bone study. **Results:** The Monte Carlo simulation demonstrated that convergence was reached within relatively few (10–15) iterations. Photon energy recovery led to a considerable quantitative improvement because the mean error between the photopeak energy window image and the true unscattered image was equal to 8.72 s.d. (the mean error between one image and the true image was the mean of the differences between the two images; the difference is expressed as several s.d., where s.d. was the square root of the true value), whereas the mean error between the 140-keV PER image and the true unscattered image was only equal to 2.70. Moreover, the true and PER spectra were highly correlated. The real phantom data pointed out that the counts in the 140-keV PER image calculated from the images acquired "with scatter" were not very different from the true counts given by the "scatter-free" reference image. Planar pelvic bone scintigraphy demonstrated the advantages of PER because contrast increased when only unscattered photons were selected. **Conclusion:** Photon energy recovery is a stable and automated method that allows recovery of the correct value of the photon energy after a scintigraphic acquisition. Its ability to separate scattered from unscattered events has been quantitatively validated.

Key Words: scatter correction; spectral deconvolution; SPECT

J Nucl Med 1998; 39:555–562

One of the major limitations of gamma cameras is their relatively poor energy resolution. In fact, the spectral response of the detector is not a Dirac distribution but a Gaussian one. At 140 keV, the gamma energy of ^{99m}Tc, the energy resolution is slightly less than 10% on modern gamma cameras. This imposes the use of relatively wide photopeak energy windows to collect most of the photons of interest, that is, the primary

Received Nov. 21, 1996; revision accepted May 8, 1997.

For correspondence or reprints contact: Pascal P. Hannequin, MD, PhD, Centre d'Imagerie Nucléaire, 4, Chemin de la Tour de la Reine, 74000 Annecy, France.

photons, and makes it difficult to resolve photons of nearly equal energies.

As a consequence, these wide photopeak energy windows include a high proportion of photons with an energy different from the photopeak energy, i.e., scattered photons that blur the scintigraphic image because their detected location does not correspond to their emission position. Moreover, these scattered photons confound accurate quantification of scintigraphic images. In particular, attenuation compensation and resolution correction on SPECT data when scattered photons have not been removed are inaccurate.

The energy resolution of the SPECT gamma camera has been improved by a factor of 2 (from 20% to 10%) since the first Anger gamma cameras were developed (*1*). However, it seems that the value of 10% approaches the physical limit of sodium iodide-based cameras. Thus, it appears that the most efficient way to compensate for the lack of energy resolution is to develop suitable image processing algorithms. Several such analytic procedures for scatter removal have been proposed in recent years (*2–13*). A recent comparison (*14*) of the procedures based on spectral analysis has shown that factor analysis methods (*15,16*) are quantitatively accurate. However, only a few of the proposed procedures are actually applied to routine nuclear medicine. In fact, most of these methods are not fully automated and are often difficult to implement. Moreover, their aim is the elimination of scattered photons rather than the improvement of the energy resolution.

We propose an original method to restore the true energy spectrum and to select the photons according to their true energy. It is based on an adapted deconvolution of the spectrum using Gaussian energy impulse responses. This procedure is called photon energy recovery (PER).

MATERIALS AND METHODS

Theory of PER

The detected spectrum (DS) is the result of the convolution of the real spectrum (RS) with the energy impulse response (EIR) of the detector. Because the FWHM of the EIR changes with energy, it was assumed that DS is a linear combination of several responses called EIR_e, which is the EIR of the photons of energy e. The value of this function at energy E was $EIR_e(E)$. It was a Gaussian function with a mean equal to e. The energy resolution r was defined as the ratio FWHM/e, where FWHM was the FWHM of the Gaussian function. Because the s.d. of a Gaussian function was equal to FWHM/c, the s.d. of EIR_e would be equal to (er)/c, where c is the constant $2[2\log(2)]^{1/2}$.

The EIR_e values included in the linear combination were those that significantly contribute to the photopeak energy window, the energy limits of which were L and H (L is the lower limit and H is the upper limit). It was considered that a EIR_e significantly contributed to the photopeak energy window when e + re was greater than L or when e − re was less than H.

The lowest limit l for e was such that:

$$l + rl = L \rightarrow l = L/(1 + r). \qquad \text{Eq. 1}$$

The highest limit h for e was such that:

$$h - rh = H \rightarrow h = H/(1 - r). \qquad \text{Eq. 2}$$

In practice, l and h were estimated with the nearest integer solutions to Equations 1 and 2. It can then be written:

$$DS(E) = \sum_{e=l}^{h} a_e EIR_e(E). \qquad \text{Eq. 3}$$

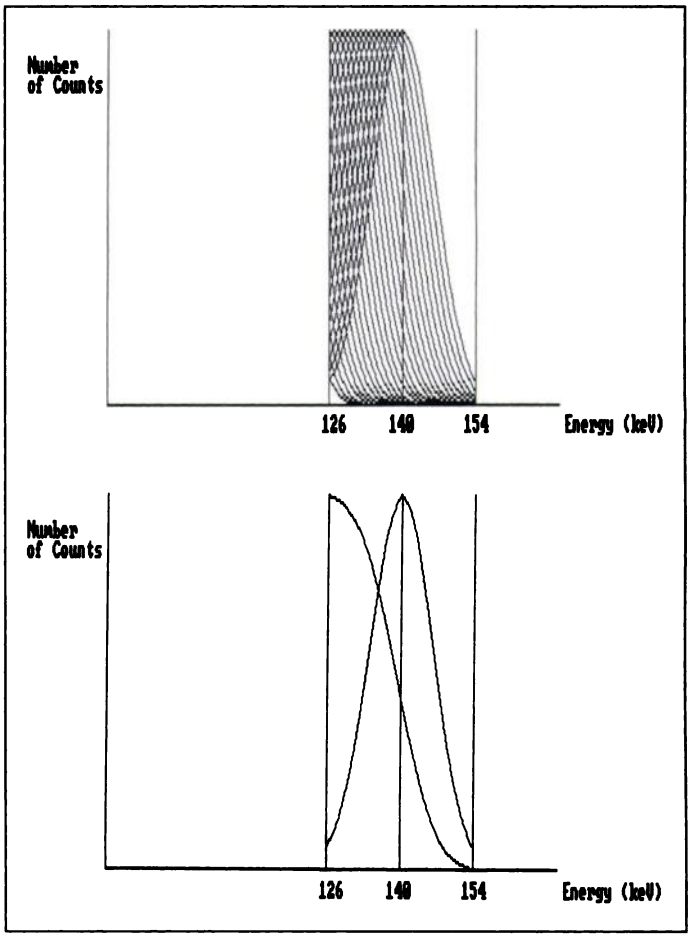

FIGURE 1. (Top) Plot of the EIR integrated in the linear combination (Eq. 6) for ^{99m}Tc. (Only the responses of the even energy values are shown). (Bottom) Plot of the two functions included in Equation 7 for ^{99m}Tc. The first function is the nonweighted sum of the responses from 115 to 139 keV, and the second function is the response at 140 keV.

For example, with ^{99m}Tc and an energy resolution of 10%, the limits L and H of the photopeak energy window were 126 and 154 keV, respectively, resulting in the following values for l and h:

$$l = 126/(1 + 0.1) = 115 \text{ keV} \qquad \text{Eq. 4}$$

and

$$h = 154/(1 - 0.1) = 171 \text{ keV}. \qquad \text{Eq. 5}$$

Considering that no photon with an energy greater than 140 keV can be emitted, Equation 3 can be written:

$$DS(E) = \sum_{e=115}^{140} a_e EIR_e(E). \qquad \text{Eq. 6}$$

The EIR_e values included in Equation 6 are shown in Figure 1 (top).

The estimation of a_e could have been performed with a multiple linear regression (*17*). However, there was a high correlation between the EIR_e values due to large overlaps, as shown in Figure 1 (top). Then, the expression in Equation 5 could not be considered as a set of linearly independent equations. One solution to this problem of colinearity was to reduce the number of equations (*18–20*). In PER, we chose an original approach, which consists of performing recursive linear regressions using only two variables in the following way.

Recursive Process. At the first step, DS was called ^{h}DS and was assumed to be the weighted sum of only two energy functions

[Fig. 1B (bottom)]. The first function was the sum of the EIR_e from l to h−1, and the second function was EIR_h:

$$^{h}DS = {}^{h}\alpha \sum_{e=l}^{h-1} EIR_e + {}^{h}\beta EIR_h. \quad \text{Eq. 7}$$

A two-dimensional linear regression is performed and the parameters $^{h}\alpha$ and $^{h}\beta$ are estimated. Because the second function was EIR_h, it is assumed that $^{h}\beta$ was an estimation $\hat{a}_h$ of a_h. The component of energy h was then removed from DS in the following way:

$$^{h-1}DS = {}^{h}DS - {}^{h}\beta EIR_h, \quad \text{Eq. 8}$$

where ^{h-1}DS was the DS without the component of energy h.

At the jth step of this recursive process:

$$^{j}DS = {}^{j+1}DS - {}^{j+1}\beta EIR_{j+1}, \quad \text{Eq. 9}$$

where ^{j}DS is the DS without the components of energy h,h−1,... ,j+1.

The two-dimensional linear regression was performed on ^{j}DS according to the following equation:

$$^{j}DS = {}^{j}\alpha \sum_{e=l}^{j} EIR_e + {}^{j}\beta EIR_j. \quad \text{Eq. 10}$$

At the end of this recursive process, all the a_e from h to l+1 had been estimated.

Iterative Process. During this first estimation of the a_e, it was assumed, in the first function of Equations 7 and 10, that all the EIR_e values had the same weight. This assumption was not correct because the EIR_e must be precisely weighted by the a_e. One solution was to estimate the a_e by iterating the recursive process.

At the first step, the weights of the EIR_e were set equal to 1, as described in the previous section for Equations 7 and 10. At the mth step, the weights of the EIR_e were the estimated values of the a_e at step m−1, and Equations 7 and 10 became:

$$^{h}DS = {}^{h}\alpha \sum_{e=l}^{h-1} {}^{m-1}\hat{a}_e EIR_e + {}^{h}\beta EIR_h \quad \text{Eq. 11}$$

and

$$^{j}DS = {}^{j}\alpha \sum_{e=l}^{j} {}^{m-1}\hat{a}_e EIR_e + {}^{j}\beta EIR_j, \quad \text{Eq. 12}$$

where $^{m-1}\hat{a}_e$ is the estimation of a_e at step m−1. Because a_l was not estimated in the recursive process, it was assumed that at step m, $^{m}\hat{a}_l$ was equal to $^{m}\hat{a}_{l+1}$.

At the end of each step of this iterative process, it was possible to calculate a reconstructed spectrum (^{m}RS) according to the following equation:

$$^{m}RS = \sum_{e=l}^{h} {}^{m}\hat{a}_e EIR_e. \quad \text{Eq. 13}$$

The error between this reconstructed spectrum ^{m}RS and the DS was calculated:

$$\text{error} = \sum_{E=L}^{H} \text{ABS}(^{m}RS(E) - DS(E)). \quad \text{Eq. 14}$$

The iterative process was stopped when this error did not decrease anymore between two successive iterations.

Implementation

In the previous section, the process for one pixel was described. In practice, this process must be repeated for all the pixels in the image. Then, the results of PER were a series of energy-dependent images, with energies ranging from l+1 to h.

In the case of ^{99m}Tc, the 140-keV image was the estimation of the image due to unscattered photons, whereas the other images were associated with the scattered photons ranging from 139–116 keV.

Width of Channels for the Energy Variable E. Because all the linear regressions were performed on sets of two equations, it was not necessary to use a large number of intervals for the energy detection in the photopeak window L–H. In practice, for the acquisition facilities available on our gamma camera (DSX Gamma Camera; SMV), only four subwindows are used. When using ^{99m}Tc, the detection is made in the four energy channels as follows: channel 1, 126–132 keV; channel 2, 133–140 keV; channel 3, 141–147 keV; and channel 4, 148–154 keV.

Width of Channels for the Energy Variable e. The recursive process is performed from h to l+1. The width of the energy channel e can be chosen among values ranging from 1 keV to several keV, except for h, which must always be considered in a 1-keV channel because it represents the photopeak energy in most applications. The advantage of reducing the number of channels is that it decreases processing time. The drawback is the increase in approximation errors on the shape of the EIR_e. In fact, when the width of the energy channel e is equal to several keV, the EIR_e is considered to be the sum of the energy responses of 1-keV increments within the channel, whereas it is actually a weighted sum of these 1-keV responses.

Determination of the Energy Impulse Responses. As described in the previous section, for each energy step e, the corresponding EIR_e is a Gaussian function with a mean equal to e and a s.d. equal to (er)/c. The energy resolution r is supposed to be constant for the considered energy range.

Because these EIR_e values are theoretical, it must be checked that there is a good fit between these values and the true energy response of the detector. This checking was performed using a point source of the considered radionuclide in air, and its true spectrum was compared with the EIR_e of its photopeak energy. When an offset was found, it was corrected not only on the photopeak EIR_e values but also on all the lower energy EIR_e values included in the linear combination.

Number of Iterations. For a given pixel, the iterative process was stopped when the error defined in Equation 14 was sufficiently stable. Stability was defined as no further decrease during four successive iterations.

In this way, the number of iterations could vary from one pixel to another. However, for all the pixels, the same maximal number of iterations was imposed.

The algorithm was implemented on a PC system (clock speed = 100 Mhz; RAM = 16 Mbyte) using PDS language. Processing time was 3 min for a 64 × 64 image, using a maximal number of 10 iterations and e channel width of 2 keV.

Validation

Monte Carlo Simulation. Monte Carlo simulation (*21–23*) was performed as described previously (*15*). A point source was contained in a cylindrical water phantom. The diameter of the cylinder was 14 cm, and the height was 20 cm. The distance between the point source and the detector was 10 cm. The energy resolution of the detector was assumed to be equal to 0.1 (10%). All the photons detected in the 126–154 keV window were collected.

Each detected photon was stored twice, once in the true energy series and once in the simulated acquisition energy series:

1. The true energy series contained 26 images of 1-keV width, from 115–140 keV. Each photon was stored in one image of this series according to its true energy.
2. The simulated acquisition energy series contained four images recorded in the four subwindows, as described in the previous section. Each photon was stored in one image of this series according to its energy of detection, i.e., after the 10% energy degradation. The sum of this series was the conventional 126- to 154-keV image used for ^{99m}Tc. Photon energy recovery was then applied to this simulated energy series. The resulting energy series (or images) obtained after PER processing will be referred to as the PER series (or the PER images).

A total number of 250,000 photons was collected. The format of the images was 64 × 64 with a pixel size of 0.9 × 0.9 cm^2.

The quantitative performances of PER were first tested by comparing the 140-keV image of the PER series with the 140-keV image of the true series. The value of the pixel i in the 140-keV PER image was $\hat{u}_{140}(i)$, and $u_{140}(i)$ was its value in the 140-keV image of the true series. Considering the characteristics of the noise in the scintigraphic data (the s.d. of the distribution is equal to the square root of the mean) the error on $\hat{u}_{140}(i)$ could be measured by the ratio:

$$\text{error}(i) = \frac{\text{ABS}(\hat{u}_{140}(i) - u_{140}(i))}{(u_{140}(i))^{1/2}}, \qquad \text{Eq. 15}$$

when $u_{140}(i) > 0$.

The ratio error(i) is thus expressed as several s.d. This ratio was measured for each pixel of the image and was plotted according to the true value $u_{140}(i)$.

The quantitative performances of PER were then evaluated by comparing the PER spectrum with the true spectrum. For each pixel, the coefficient of correlation r(i) between its spectrum estimated by PER and its true spectrum was calculated, and the weighted mean r_m of these coefficients on the whole image was obtained by the following equation:

$$r_m = \frac{\sum_{i=1}^{4096} r(i) \sum_{e=115}^{140} u_e(i)}{\sum_{i=1}^{4096} \sum_{e=115}^{140} u_e(i)}. \qquad \text{Eq. 16}$$

To select the optimal value for the maximal number of iterations and for the width of the e channel, PER was performed several times on the simulated acquisition series. The tested values were 1, 5, 10, 15 and 25 for the maximal number of iterations and 2 keV, 3 keV and 4 keV for the width of the e channel.

Real Phantom. This phantom was made of four tubes, filled with 2 ml of a ^{99m}Tc solution, that were positioned 1 cm apart and away from the border of a parallelipiped, filled with another ^{99m}Tc solution. The volume of the parallelipiped was 4 liters. The radioactive concentration in the parallelipiped was 37 MBq/liter. The radioactive concentration varied from 92.5–370 MBq/liter in the four tubes. The phantom lay on a table, with the gamma camera beneath.

Two acquisitions were performed (Fig. 2): one with only the four tubes ("without scatter" acquisition) and one with the four tubes and the parallelipiped ("with scatter" acquisition). The tubes were not displaced from one acquisition to the other. Each acquisition was performed for 10 min, in 64 × 64 format, on a DSX SMV gamma camera, using the four energy subwindows described above. The sum images of the four subwindows were the conventional 126- to 154-keV images.

Photon energy recovery was only performed on the "with scatter" acquisition series, using a width of 2 keV for e channel and a maximum of 10 iterations. With the resulting PER series, six cumulative images with spectral window of increasing width were generated. These spectral windows were: 140 keV, 138–140 keV, 136–140 keV, 130–140 keV, 124–140 keV and 115–140 keV. The first image was the PER-estimated image of the unscattered photons. The other images obviously included an increasing amount of scattered photons. The last image contained all the photons from 115 to 140 keV and was assumed to be close to the conventional 126- to 154-keV image.

A rectangular region of interest (ROI) was drawn on each of the four tubes. The density of counts in the four ROIs was calculated for the six cumulative images and for the reference image, which is the conventional 126- to 154-keV image of the "without scatter" acquisition.

Scintigraphic Images. PER was illustrated clinically using a ^{99m}Tc bone scintigram. A posterior image of the pelvis was acquired 2 hr after the injection of 555 MBq ^{99m}Tc-hydroxymethylene diphosphonate, using a parallel high-resolution collimator (HR BE DSX collimator). The acquisition time was 10 min, in 64 × 64 format, on a DSX SMV gamma camera using the four energy subwindows described above.

Photon energy recovery was applied using 10 iterations and an e channel width of 2 keV. Six cumulative images were generated in the same way as for the real phantom. For each of these cumulative images, a transverse profile of counts per pixel was displayed.

RESULTS

Monte Carlo Simulation

Table 1 gives the results of the Monte Carlo simulation as a function of the width of the e channel and as a function of the maximal number of iterations.

Table 1 indicates that the three numeric parameters are not very different among the three channel widths. However, the best values were always obtained for a width of 2 keV.

It also shows that the iterative process converges well because optimal values for the three parameters were obtained for a maximal number of 10 or 15 iterations. Furthermore, the process was stable because no further change in the values of the three parameters was observed, even for a maximal number of 25 iterations.

As far as the mean error and the total number of counts were concerned, the values in Table 1 must be compared with the values concerning the conventional 126- to 154-keV image. The mean error between the conventional 126–154 keV image and the true 140-keV image was equal to 8.71 s.d. The number of counts in the conventional 126- to 154-keV image was equal to 136% of the total number of counts in the true 140-keV image.

Figure 3 shows the evolution of the errors (the reference is the true 140-keV image obtained by Monte Carlo simulation), from the conventional 126- to 154-keV image (filled squares) to the 140-keV PER image (open squares), obtained after a maximal number of iterations of 10. The circles are for the 140-keV PER image obtained at the first step of PER processing. It indicates that PER allows one to obtain an estimation of the 140-keV distribution with an error of 2 or 3 s.d., whereas the initial error in the conventional 126- to 154-keV image is always greater than 8 s.d. when the number of counts is superior

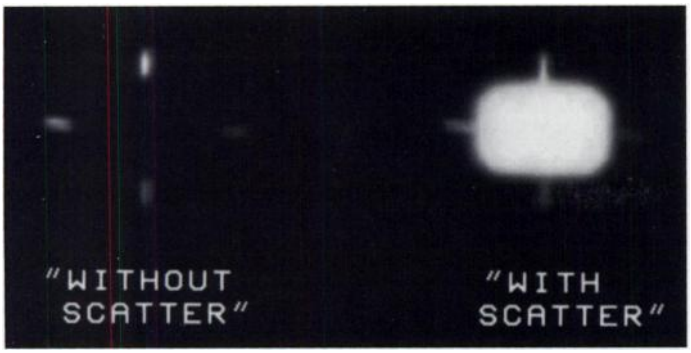

FIGURE 2. Scintigraphic images of the real phantom. (Left) "Without scatter" acquisition. Only the four tubes are placed on the table. (Right) "With scatter" acquisition. The four tubes and the parallelipiped are placed on the table.

to 30. Figure 3 also shows the significant decrease in the error between a maximal number of iterations of 1 and 10.

Real Phantom

Table 2 gives the counts density in the four tube ROIs for the six cumulative PER images obtained from the with scatter acquisition in percentage of the true density given by the conventional 126- to 154-keV image acquired without scatter. This table indicates that the percentage logically decreases from the 115- to 140-keV image to the 140-keV image. In this 140-keV image, it can be considered that the correct proportion of scattered photons has been removed because the percentage of counts in the four ROIs varied from 97.85% to 104.1% of the true values; the difference from 100% is due to statistical fluctuations.

Scintigraphic Evaluation

Figure 4 clearly shows that the contrast increases when the width of the spectral window decreases in the cumulative PER images. The best contrast is logically obtained with the 140-keV PER image, as shown by the horizontal profile, which is drawn tangentially to the lowest edge of the bladder. The blurring effect of scattering is easily observable on the hot spot located on the sacrum between the lower part of the two sacro–iliac joints. The edges of this hot spot became indistinct, and its size increased when the width of the window became larger. The 115- to 140-keV image is not supposed to be significantly different from the usual 126- to 140-keV image.

Figure 4 also shows that the statistical noise increases when the width of the window decreases. In fact, the total number of kilocounts varied from 650 in the 140-keV PER image to 1208 in the 115- to 140-keV PER image.

DISCUSSION

We have developed an original algorithm for recovering the true value of photon energy in scintigraphic detection. This algorithm is based on a spectral deconvolution approach but it uses linear regression to include the dependence of the response functions on energy.

Spectral deconvolution has already been proposed in nuclear medicine for scatter correction (*24,25*), but no practical solution has been implemented on gamma cameras. This may be due to the instability of the resulting system of equations (ill-posed problem), which makes it necessary to use regularization methods. These methods impose choosing regularization parameters and are too involved in practice.

The main reason for the instability of spectral deconvolution is the high number of correlated responses, which are included in the system of equations, as shown in Figure 1 (top). A simple way to transform an ill-posed problem into a well-posed problem is to reduce the number of variables (*18–20*). For instance, this may be done using a multivariate analysis method such as principal component analysis (*26*). In PER, we use a simpler solution corresponding to iterative linear regression of only two unknown variables. The aim of the iterative process is to adjust the shape of the two energy-dependent functions included in the linear combination with their true shape, which is unknown at the beginning of the processing. Monte Carlo simulation has shown that this iterative process converges well for a small number of iterations.

The Monte Carlo results have also demonstrated the quantitative performances of PER, which reduces the mean error due to scatter in the scintigraphic image from more than 8 s.d. (8.71 in the conventional 126- to 154-keV image) to less than 3 s.d.

TABLE 1
Quantitative Results of the Monte Carlo Simulation as a Function of the Width of the e Channel and of the Maximum Number of Iterations

	MNI				
e channel width (keV)	1	5	10	15	25
Mean error*					
2	3.79	2.86	2.71	2.70	2.70
3	3.79	3.19	2.97	2.99	2.99
4	3.79	3.34	3.39	3.39	3.39
Number of counts†					
2	105.45	98.77	98.43	98.52	98.52
3	105.45	99.12	98.45	98.90	98.90
4	105.45	99.64	98.62	98.52	98.52
Mean correlation coefficient‡					
2	0.914	0.917	0.921	0.924	0.924
3	0.910	0.913	0.919	0.922	0.922
4	0.909	0.909	0.908	0.910	0.910

*Mean error between the 140-keV PER image and the true 140-keV image, expressed in number of s.d.

†Total number of counts in the 140-keV PER image expressed in percentage of the total number counts in the true 140-keV image without any normalization.

‡Mean correlation coefficient between the PER spectrum and the true spectrum.

MNI = maximal number of iterations.

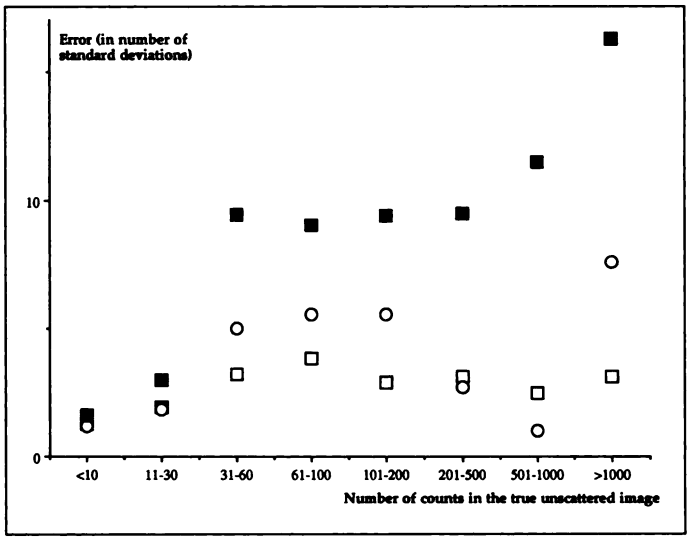

FIGURE 3. Monte Carlo simulation plot of the errors (expressed as numbers of s.d.) between the PER 140-keV image values and the true 140-keV image values against the true 140-keV image values. The errors are expressed in number of s.d. Circles, the PER image at the first iteration. Open squares, the PER image obtained with a maximal number of iterations of 10. Filled squares, the usual 126- to 140-keV image.

TABLE 2
Quantitative Results of the Real Phantom

PER cumulative image	Tube 1	Tube 2	Tube 3	Tube 4
Counts density*				
140 keV	97.85	102.75	104.11	98.81
138–140 keV	107.40	107.41	113.20	109.79
136–140 keV	117.11	111.18	122.23	117.80
130–140 keV	120.53	113.78	129.08	122.75
124–140 keV	121.60	115.16	133.20	126.01
115–140 keV	121.86	117.15	136.47	128.98

*The counts density in the PER images is expressed in percentage of the corresponding density in the "without scatter" reference image.

(2.70 in the 140-keV PER image). Moreover, Figure 3 indicates that this level of error, which is just above the statistical noise level, seems to be count-independent.

Table 1 indicates that PER preserves the total number of counts in the image; this is confirmed with the real phantom (Table 2, first line) because the count densities in the four ROIs of the 140-keV PER image are quite similar to those in the four ROIs of the without scatter reference image. In fact, the percentage in the four ROIs progressively diverges from the 100% reference value when the width of the spectral window increases.

The qualitative improvement in overall image quality associated with PER are illustrated by the bone scintigrams in Figure 4. The horizontal counts profiles clearly demonstrate the contrast improvement in the 140-keV PER image by comparison with the 115- to 140-keV PER image, which is comparable to the conventional 126- to 154-keV image. The contrast regularly decreases when the width of the spectral window becomes larger, due to the integration of photons with an increased scattering angle. That is also shown by the modification of the shape of the hot spot located in the upper part of the sacrum. Figure 4 also indicates that noise level increases when scatter photons are removed. However, PER allows one to choose a cutoff value for the selection of photons in the so-called scatter-free image. In most cases, this cutoff value is that of the photopeak energy (140 keV for ^{99m}Tc), but it can be lower when the noise increases too much in the scatter-free image. In this way, the user can balance the statistical noise level and the Compton blurring.

Photon energy recovery is not actually a scatter correction method but rather a physical approach for improving the effective energy resolution of gamma cameras. In this way, PER allows a better discrimination of the photons according to their energy. The main application of PER is, in fact, to select the unscattered photons among all the acquired photons to obtain a scatter-free image. However, other applications can be considered, such as discrimination between two radionuclides with nearly equal photopeak energy in simultaneous dual-radionuclide imaging or attenuation correction procedures using external sources with a photopeak energy close to the injected radionuclide energy.

Photon energy recovery has several advantages over other methods of scatter correction. First, PER respects the hypothesis of nonstationarity of Compton scattering, whereas several Compton correction methods, such as dual-energy window (*3*) and triple-energy window (TEW) (*13*), are stationary procedures. Compton-free imaging (*12*) is also a nonstationary procedure, which assumes that the DS can be fitted by a sum of scatter spectral functions given by the Klein–Nishina equations and integration of the EIR of the detector. However, as for spectral deconvolution procedures (*24,25*), the main limit is the instability of the system of equations, due to a large number of highly correlated functions and to the high statistical noise (the procedure is performed on a 1-pixel basis and uses very narrow spectral windows). The limit is the same for factor analysis of medical images using target–apex seeking (FAMIS-TAS) (*16*), which uses a three-factor model to respect the stationarity hypothesis. This model is adequate for the factor extraction procedure, which is performed after pixel clustering but is not valid for the factor images construction, which is performed in the initial sampling, with a higher statistical noise.

The multienergy window acquisition technique (*8*) assumes that the scatter component in the photopeak energy window is the result of a weighted sum of contributions from different spectral windows. Each element of the sum is the convolution of an image recorded in a spectral window with a spatial transfer function adapted to this given spectral window. The main difficulty of this procedure is estimating the transfer functions, which must be recalculated at each acquisition, according to the patient geometry.

Another advantage of PER is that it does not require very narrow spectral windows, such as the 2-keV windows used in TEW. These narrow windows generate high statistical noise because subtraction is generally performed on a 1-pixel basis. Moreover, PER does not require sophisticated acquisition procedures, such as list mode acquisition (*16*), which is used in factor analysis of medical images using target–apex seeking. Furthermore, PER is a physical approach that does not impose an empirical model, as does the trapezoidal interpolation in TEW, and that does not introduce numerical parameters (magic numbers), as does holospectral imaging (*9*). In fact, the aim of PER is not to model the RS but to estimate it; the model is for the DS. The advantage of PER over other Compton correction methods is precisely to make no hypothesis about the shape of the Compton spectrum and, in fact, PER can be extended to all detection situations in which a RS must be estimated from a DS. The RS can be any spectrum, including or not including Compton scattered photons. Finally, PER is performed on the whole image, requiring no ROI selection.

In practice, the width of the e channel and the number of subwindows must be adapted to each gamma camera, depending on acquisition facilities and on calculation capacity.

The user must be careful in checking the adequacy between the real energy response of his gamma camera and the theoretical EIR in the chosen subwindows. Usually this verification can only be made for a small number of energy values, due to the limited number of available radionuclides. However, when an offset is found for one energy value, it is easy to extrapolate and to correct this offset for the other energies, the theoretical responses of which are known. In practice, the verification is performed on the photopeak of the considered radionuclide by using a point source in air.

This emphasizes the need of quality control on gamma cameras. However, PER does not require energy quality control outside the conventional photopeak energy windows, whereas several proposed methods for scatter correction need it because low-energy photons are also acquired (*3,7–9,11,12,15,16*).

In this study, only 64 × 64 planar images were processed. It would be necessary to test PER in finer matrix images and, above all, on SPECT projections. In fact, one of the major interests of scatter correction is to make the projections more consistent with the hypothesis of SPECT algorithms. Scatter correction eliminates backprojection of inaccurate data and allows one to apply attenuation and spatial resolution correc-

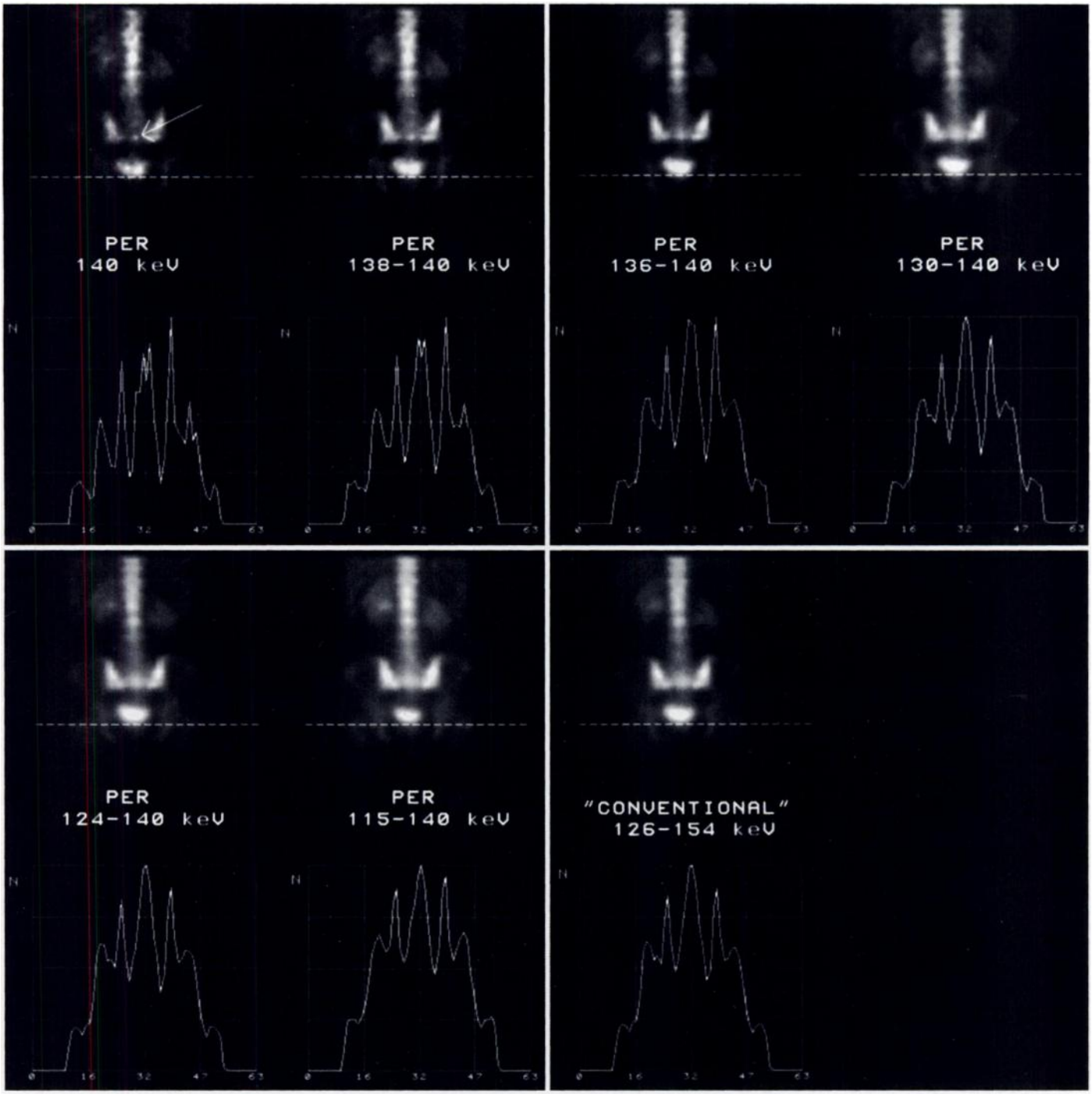

FIGURE 4. Scintigraphic reconstruction of different cumulative PER images using different energy windows. The 140-keV PER image is the estimation of the true photopeak image. Each image is presented with a horizontal count profile. Arrow, the hot spot, becomes indistinct when the width of the spectral window becomes larger.

tions on unscattered photons. In practice, selection of the unscattered photons is probably the first processing to apply on the projections. Photon energy recovery is well-adapted to this projection correction because it is automated and can be performed on the fly, as soon as a projection has been acquired and before the end of the whole acquisition.

Only ^{99m}Tc has been considered in this work, but PER can be applied to all radionuclides, including positron emitters, because no hypothesis concerning the gamma emissions is made. The only adaptation for a given photopeak window concerns the upper limit for energy variable e, depending on whether photons are emitted at higher energies (multipeak emissions).

CONCLUSION

Photon energy recovery is an automated method to select the photons acquired in a given window according to the value of their true energy. Photon energy recovery enables a significant reduction of the errors due to scatter. Its performance has been quantitatively checked using Monte Carlo simulation and real phantom data for planar images. This method must now be investigated for SPECT studies.

REFERENCES

1. Mestais C, Allemand R, Peyret O, Tournier E. Les compromis physiques de la détection nucléaire: incidence sur la conception des caméras. *Med Nucl* 1994;18:303–309.

2. Axelsson B, Msaki P, Israelsson A. Subtraction of Compton-scattered photons in single photon emission computerized tomography. *J Nucl Med* 1984;25:490–494.
3. Jaszczak R, Greer KL, Floyd CE, Harris CC, Coleman RE. Improved SPECT quantification using compensation for scattered photons. *J Nucl Med* 1984;25:893–900.
4. Floyd CE, Jaszczak RJ, Greer KL, Coleman RE. Deconvolution of Compton scatter in SPECT. *J Nucl Med* 1985;26:403–408.
5. Halama JR, Henkin RE, Friend LE. Gamma camera radionuclide images: improved contrast with energy-weighted acquisition. *Radiology* 1988;169:533–538.
6. Msaki P, Axelsson, B, Dahl CM, Larsson SA. A generalized scatter correction technique in SPECT using point scatter distribution functions. *J Nucl Med* 1987;28: 1861–1869.
7. Koral KF, Wang X, Rogers WL, Clinthorne NH, Wang X. SPECT Compton-scattering correction by analysis of energy spectra. *J Nucl Med* 1988;29:195–202.
8. Gilardi MC, Bettinardi V, Todd-Pokropek A, Milanesi L, Fazio F. Assessment and comparison of three scatter correction techniques in single photon emission computed tomography. *J Nucl Med* 1988;29:1971–1979.
9. Gagnon D, Todd-Pokropek A, Arsenault A, Dupras G. Introduction to holospectral imaging in nuclear medicine for scatter subtraction. *IEEE Trans Med Imaging* 1989;8:245–250.
10. Ljungberg M, Strand SE. Scatter and attenuation correction in SPECT using density maps and Monte Carlo simulated scatter functions. *J Nucl Med* 1990;31:1560–1567.
11. King MA, Hademenos GJ, Glick SJ. A dual-photopeak window method for scatter correction. *J Nucl Med* 1992;33:605–612.
12. Maor D, Berlad G, Chrem Y, Voil A, Todd-Pokropek A. Klein-Nishina based energy factors for Compton-free imaging (CFI) [Abstract]. *J Nucl Med* 1991;32:1000.
13. Ichihara T, Ogawa K, Motomura N, Kubo A, Hashimoto S. Compton scatter compensation using the triple energy window method for single and dual isotope SPECT. *J Nucl Med* 1993;34:2216–2221.
14. Buvat I, Rodriguez-Villafuerte M, Todd-Pokropek A, Benali H, Di Paola R. Comparative assessment of nine scatter correction methods based on spectral analysis using Monte Carlo simulations. *J Nucl Med* 1995;36:1476–1488.
15. Mas J, Hannequin P, Ben Younes R, Bellaton B, Bidet R. Scatter correction in planar imaging and SPECT by constrained factor analysis of dynamic structures (FADS). *Phys Med Biol* 1990;35:1451–1465.
16. Buvat I, Benali H, Frouin F, et al. Target apex-seeking in factor analysis of medical image sequences. *Phys Med Biol* 1993;28:123–138.
17. Weisberg S. *Applied linear regression*. New York: Wiley; 1985:124.
18. Hocking RR. The analysis and selection of variables in linear regression. *Biometrics* 1976;32:1–49.
19. Thompson M. Selection of variables in multiple regression. Part I: a review and evaluation. *Int Stat Rev* 1978;46:1–19.
20. Thompson M. Selection of variables in multiple regression. Part II: chosen procedures, computation and examples. *Int Stat Rev* 1978;46:129–146.
21. Beck JW, Jaszczak RJ, Coleman RE, Starmer CF, Nolte LW. Analysis of SPECT including scatter and attenuation using sophisticated Monte Carlo modeling methods. *IEEE Trans Nucl Sci* 1982;NS-29:506–511.
22. Floyd CE, Jaszczak RJ, Harris CC, Coleman RE. Energy and spatial distribution of multiple order Compton scatter in SPECT: a Monte Carlo investigation. *Phys Med Biol* 1984;29:1217–1230.
23. Floyd CE, Jaszczak RJ, Harris CC, Greer KL, Coleman RE. Monte Carlo evaluation of Compton scatter subtraction in single photon emission computed tomography. *Med Phys* 1985;12:776–778.
24. Ben Younes R, Mas J, Pousse A, Bidet R. Compton scatter correction by spectral iterative deconvolution [Abstract]. *Eur J Nucl Med* 1991;18:541.
25. Wang X, Koral KF. A regularized deconvolution-fitting method for Compton-scatter correction in SPECT. *IEEE Trans Med Imaging* 1992;11:351–360.
26. Palm R, Iemma AF. Quelques alternatives à la régression classique dans le cas de la colinéarité. *Rev Stat Appl* 1995;43:5–33.

A Comparison of 180° and 360° Acquisition for Attenuation-Compensated Thallium-201 SPECT Images

Karen J. LaCroix, Benjamin M.W. Tsui and Bruce H. Hasegawa

Department of Biomedical Engineering and Department of Radiology, The University of North Carolina at Chapel Hill, Chapel Hill, North Carolina; and The Bioengineering Graduate Group and Department of Radiology, University of California, San Francisco, California

This study compared attenuation compensated, myocardial SPECT images reconstructed from 180° and 360° data to determine if either data acquisition method might yield improved image quality. Specifically, this study analyzed how the use of either 180° or 360° data affects: (a) the relative count density distribution, (b) defect contrast and (c) level of statistical noise in the left ventricular (LV) wall in the reconstructed SPECT images. **Methods:** Using the three-dimensional MCAT phantom simulating ^{201}Tl uptake in the upper torso and the SIMSET Monte Carlo code, noise-free projection datasets for both 180° (45° LPO to 45° RAO) and 360° acquisition were generated with the effects of nonuniform attenuation, collimator-detector response and scatter. In addition, low-noise experimental phantom data were acquired over 180° and 360°. Assuming the same total acquisition time, four sets of noisy projection data were simulated from scaled noise-free, simulated data for the following acquisitions: (a) 180° and (b) 360° data acquired on a 90° dual-detector system and (c) 180° and (d) 360° data acquired on a 120° triple-detector system. For each of the four acquisition schemes, 400 realizations of noisy projection data were generated, and the normalized s.d. in the reconstructed images was calculated for five ROIs in the LV wall. Images were reconstructed with nonuniform attenuation compensation using ML-EM algorithm for 25, 50 and 75 iterations. **Results:** Both the simulated noise-free and experimental low-noise images reconstructed from 180° and 360° data showed nearly identical count densities and defect contrasts in the LV wall. For the 90° dual-detector system, 180° images showed less noise, while for the 120° triple-detector system, 360° showed less noise; however, these differences in noise level were extremely small after a smoothing filter was applied. The 180° images acquired with the 90° dual-detector system showed the same noise level as the 360° images acquired with the 120° triple-detector system, so neither system geometry had an advantage with respect to reduced noise in the SPECT images. **Conclusion:** When nonuniform attenuation compensation is included in the reconstruction, the count density in the LV wall is nearly identical for 180° and 360° SPECT images, and the 90° dual-detector and 120° triple-detector SPECT systems produced similar SPECT images for the same total acquisition time.

Key Words: SPECT; attenuation compensation; thallium-201 perfusion agents; cardiac simulation study

J Nucl Med 1998; 39:562–574

Many previous studies have compared ^{201}Tl SPECT images reconstructed from data acquired over 180°, specifically the 45° right anterior oblique (RAO) to the 45° left posterior oblique (LPO) arc, to images reconstructed from data acquired over 360° using, for reconstruction, the filtered backprojection method (*1–6*). These studies have shown that the images reconstructed from 180° data generally have better contrast and spatial resolution in the left anterior region of the patient (where

Received Dec. 2, 1996; revision accepted May 8, 1997.

For correspondence or reprints contact: Karen J. LaCroix, PhD, Dept. of Biomedical Engineering, CB #7575, 152 MacNider, The University of North Carolina at Chapel Hill, Chapel Hill, NC 27599.